JOURNAL OF MATERIALS SCIENCE **36** (2001) 4649–4659

Cracking mechanism in AlN(11$\bar{2}$0)/α-Al_2O_3(1$\bar{1}$02) heteroepitaxial films grown by MOCVD

K. KAIGAWA*, T. SHIBATA, Y. NAKAMURA, K. ASAI, M. TANAKA, H. SAKAI
NGK Insulators, Ltd., 2-56 Suda-cho, Mizuho-ku, Nagoya 467-8530, Japan
E-mail: kaigawa@ngk.co.jp

T. TSURUMI
Department of Metallurgy & Ceramics Science, Graduate School of Science & Engineering, Tokyo Institute of Technology, 2-12-1 Ookayama, Meguro-ku, Tokyo 152-8552, Japan

The cracking mechanism in AlN(11$\bar{2}$0)/α-Al_2O_3(1$\bar{1}$02) heteroepitaxial film grown by MOCVD is discussed. The crystal structure and microstructure of an AlN/Al_2O_3 film and an AlN/GaN/Al_2O_3 film are compared using high-resolution X-ray diffractometry, optical microscopy, scanning electron microscopy, and transmission electron microscopy. In the AlN/Al_2O_3 film, cracks parallel to the $[1\bar{1}00]_{AlN}$ direction and perpendicular to the interface of the film and the substrate are observed. The cracks do not propagate to the AlN film surface. The tips of the cracks are widest in the AlN film, and the cracks narrow as they penetrate deeply into the substrate. On the other hand, in the AlN/GaN/Al_2O_3 film, no cracks are observed. A concave curvature is observed in the AlN film with cracks on the Al_2O_3 substrate along the $[0001]_{AlN}$ direction, whereas a convex curvature is observed in the AlN film without cracks. On the basis of these results, the cracks, formed in the AlN film due to the tensile stress along the $[0001]_{AlN}$ direction during the epitaxial growth, propagate to the AlN film surface and into the Al_2O_3 substrate. On the other hand, in the AlN/GaN/Al_2O_3 film, it seems that the GaN buffer layer suppresses the tensile stress; as a consequence, no cracks occur. © *2001 Kluwer Academic Publishers*

1. Introduction

AlN(11$\bar{2}$0)/α-Al_2O_3(1$\bar{1}$02) heteroepitaxial film has been proposed as a piezoelectric material for gigahertz (GHz) surface acoustic wave (SAW) devices for applications in wireless communication systems because of its high SAW velocity (5910 m/s), moderate electromechanical coupling coefficient (∼1.0%), and zero temperature coefficient of delay (TCD) [1]. AlN epitaxial films on α-Al_2O_3 substrates have been grown by chemical vapor deposition (CVD) [1–14], by sputtering [15, 16] and by molecular beam epitaxy [17, 18]. The CVD method has been used more extensively than other methods, because high-quality crystals of AlN can be grown, the chemical composition can be controlled easily, and the growth rate is high. In addition, metalorganic chemical vapor deposition (MOCVD) has the advantage of being free of halide and requires only one high-temperature zone for deposition. AlN films thicker than 2 μm are required in order to obtain good physical properties for SAW devices. However, cracks which deteriorate the physical properties propagate in AlN(11$\bar{2}$0)/α-Al_2O_3(1$\bar{1}$02) heteroepitaxial films, when the films become thicker than about 1 μm. Although there have been some reports regarding the cracking and/or strain mechanisms in GaN(0001)/α-Al_2O_3(0001) heteroepitaxial films [19–25], the cracking mechanism in AlN(11$\bar{2}$0)/α-Al_2O_3(1$\bar{1}$02) heteroepitaxial films has not yet been reported.

In this study, the crystal structure and the crystallinity of the AlN(11$\bar{2}$0)/α-Al_2O_3(1$\bar{1}$02) heteroepitaxial films grown by MOCVD are evaluated using high-resolution X-ray diffractometry (HR-XRD). The surface and cross-sectional images are observed using an optical microscope (OM), a scanning electron microscope (SEM) and a transmission electron microscope (TEM). On the basis of these results, the cracking mechanism in the AlN/α-Al_2O_3 heteroepitaxial films is discussed.

2. Experimental procedure

2.1. Film growth

Two types of AlN (11$\bar{2}$0) heteroepitaxial films were grown on 3-inch-diameter α-Al_2O_3(1$\bar{1}$02) substrates of 430 μm thickness by MOCVD. One is an AlN/Al_2O_3 epitaxial film and the other is an AlN/GaN/Al_2O_3 epitaxial film with a GaN buffer layer (∼0.2 μm thick) between the AlN film and the Al_2O_3 substrate. +4° off-cut α-Al_2O_3 wafers were used as substrates in order to suppress the growth of twin AlN which cancels the piezoelectric property [26]. The +4° off-cut α-Al_2O_3 wafer is described as follows. In the case of the conventional wafer (Just-cut), the interfacial angle between

© *2001 Kluwer Academic Publishers*

the surface, which is the $(1\bar{1}02)$ plane, and the (0001) planes is 57.6°. In the case of the +4° off-cut wafer, the surface is slanted from the $(1\bar{1}02)$ plane slightly, and the interfacial angle between the surface and the (0001) plane is 61.6° (=57.6 + 4). Trimethylaluminum (TMA, $(CH_3)_3Al$) and ammonia (NH_3) were used as source gases for the AlN film, and trimethylgallium (TMG, $(CH_3)_3Ga$) and NH_3 were used for the GaN layer. The growth conditions were as follows. The substrate was first annealed in H_2 ambient, and then the initial nitriding layer was formed by heating the substrate at 1100°C in a mixed flow of NH_3 and H_2 in a horizontal reactor. Subsequently, TMA was introduced into the reactor to grow AlN epitaxial film at 15–20 Torr. The flow rates of

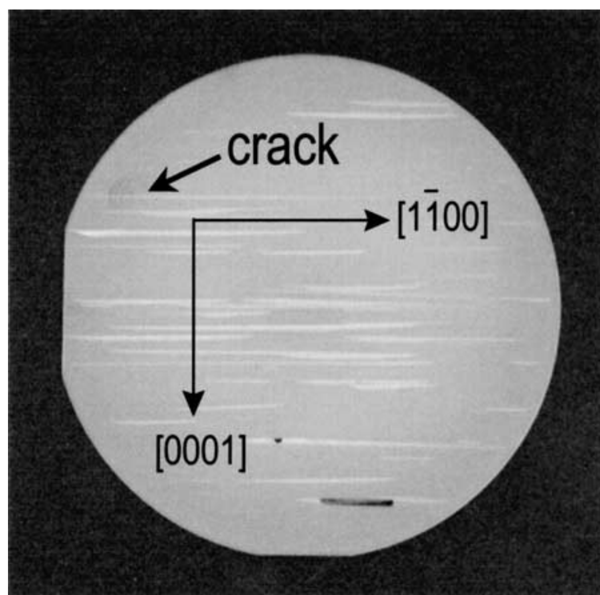

Figure 1 Surface photograph of the AlN$(11\bar{2}0)$ heteroepitaxial film on the 3-inch α-$Al_2O_3(1\bar{1}02)$ substrate. Cracks parallel to the $[1\bar{1}00]_{AlN}$ direction are observed in the AlN/Al_2O_3 film.

TABLE I Lattice mismatches and differences in thermal expansion rates for AlN and GaN on α-Al_2O_3 (1100°C–20°C)

Film system	Direction	Lattice mismatch (%)	$\Delta\alpha$: α(film) − $\alpha(Al_2O_3)$ (%)
AlN/Al_2O_3	$[1\bar{1}00]_{AlN}$	+ 13.29	− 0.24
	$[0001]_{AlN}$	− 2.85	− 0.44
GaN/Al_2O_3	$[1\bar{1}00]_{GaN}$	+ 16.09	− 0.21
	$[0001]_{GaN}$	+ 1.11	− 0.05

TMA, NH_3 and H_2 were 50 sccm, 2000 sccm and 6600 sccm, respectively. In the case of the AlN/GaN/Al_2O_3 film, TMG was introduced into the reactor after the first annealing to grow the GaN buffer layer at 15 Torr for 10 min. The flow rate of TMG was the same as that of TMA. Table I lists the lattice mismatches and the differences in the thermal expansion rates between AlN, GaN and α-Al_2O_3 [10, 27, 28]. The lattice mismatch along the $[1\bar{1}00]_{AlN,GaN}$ direction is extremely large compared with that along the $[0001]_{AlN,GaN}$ direction. The d-spacing of AlN along the $[1\bar{1}00]_{AlN}$ direction is larger than that of Al_2O_3, whereas that of AlN along the $[0001]_{AlN}$ direction is smaller. On the other hand, the d-spacings of GaN along both directions are larger than those of Al_2O_3. The thermal expansion rates of AlN and GaN are smaller than that of Al_2O_3.

The curvature of the wafers along both the $[1\bar{1}00]_{AlN}$ and $[0001]_{AlN}$ directions was measured using FORM TALYSURF (Taylor Hobson, SERIES S5).

2.2. Crystal structure analysis

The crystallinity and crystal structure of the AlN heteroepitaxial films were characterized using HR-XRD (Philips, MRD) with a two-crystal, four-reflection Bartels monochromator [29] as an incident optics and with

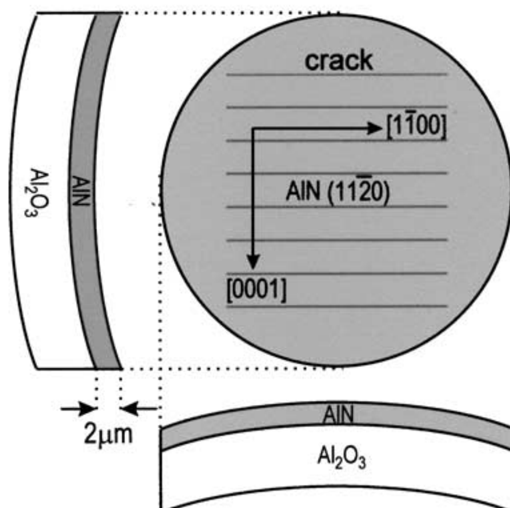

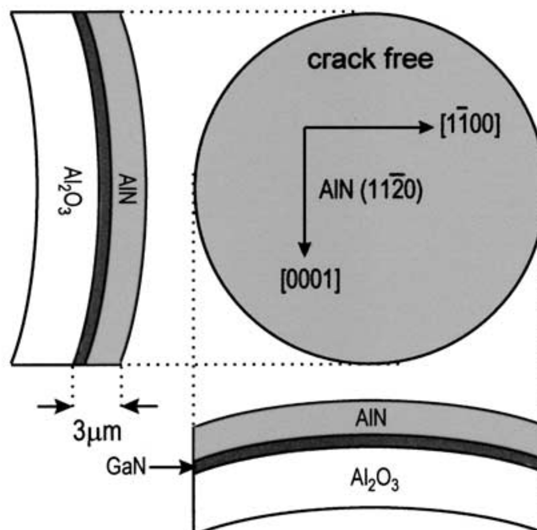

Figure 2 Schematic figures of the curvature in the AlN/Al_2O_3 epitaxial film with cracks and the AlN/GaN/Al_2O_3 epitaxial film without cracks.

a one-crystal, two-reflection analyzer as a diffracted optics. The monochromator and analyzer crystals were made from perfect Ge crystals, and were set to reflect from the (220) planes using Cu $K_{\alpha 1}$ radiation. The rocking curves and the diffraction space maps close to the $11\bar{2}0$ reflection of the AlN films were measured using the monochromator by aligning the $[0001]_{AlN}$ direction horizontal to the incident X-ray beam. The diffraction space maps were measured using both the monochromator and the analyzer. The absolute lattice constants of AlN films and α-Al_2O_3 substrates were measured by Fewster's method [30]. Additionally, X-ray powder diffraction profiles of ground specimens were measured to obtain the stress-free lattice parameters of AlN and Al_2O_3. The lattice parameters were calculated using the whole powder pattern decomposition (WPPD) method [31].

2.3. Microstructure observation

The cross-sectional AlN $(1\bar{1}00)$ images of the AlN/Al_2O_3 and $AlN/GaN/Al_2O_3$ heteroepitaxial films were obtained using a TEM operating at 200 kV (JEOL, JEM-2010). Electron diffraction patterns of the AlN films and the Al_2O_3 substrates were also taken. The ultra thin samples (about 40 nm thick) for TEM observations were prepared using a focused ion beam (FIB) at 30 kV (FEI, FIB200). In addition, the surface morphology of the AlN films was observed using an OM and a SEM at 20 kV (JEOL, JEM-6300).

3. Results and discussion

3.1. Cracks and curvature of the wafers

Cracks parallel to the $[1\bar{1}00]_{AlN}$ direction are observed in the 2-μm-thick AlN/Al_2O_3 film, as shown in Fig. 1. However, no cracks are observed in the $AlN/GaN/Al_2O_3$ film, in spite of the film thickness being about 3 μm.

After cooling to room temperature, the wafers curve as shown in Fig. 2. The wafer with cracks (AlN/Al_2O_3 film) curve concavely along the $[0001]_{AlN}$ direction but convexly along the $[1\bar{1}00]_{AlN}$ direction, indicating that tensile stress is induced along the $[0001]_{AlN}$ direction in the AlN film, whereas the compressive stress is induced along the $[1\bar{1}00]_{AlN}$ direction. The radii of curvature along the $[1\bar{1}00]_{AlN}$ and $[0001]_{AlN}$ directions are 100 m and 50 m, respectively. On the other hand, the wafer without cracks ($AlN/GaN/Al_2O_3$ film) curves in such a way that the film is convex along both the $[0001]_{AlN}$ and $[1\bar{1}00]_{AlN}$ directions, indicating that compressive stress is induced along both directions in the AlN film, as Duffy *et al*. [4] have reported. The radii of curvature along the $[1\bar{1}00]_{AlN}$ and $[0001]_{AlN}$ directions are 100 m and 200 m, respectively. Since the thermal expansion coefficients of AlN along both the $[1\bar{1}00]_{AlN}$ and $[0001]_{AlN}$ directions are smaller than those of Al_2O_3 (Table I), compressive stress should be induced along both directions in the AlN film after cooling to room temperature. Therefore, the curvature of the wafer without cracks ($AlN/GaN/Al_2O_3$ film) can be interpreted by the thermal stress. On the other hand, in the AlN/Al_2O_3

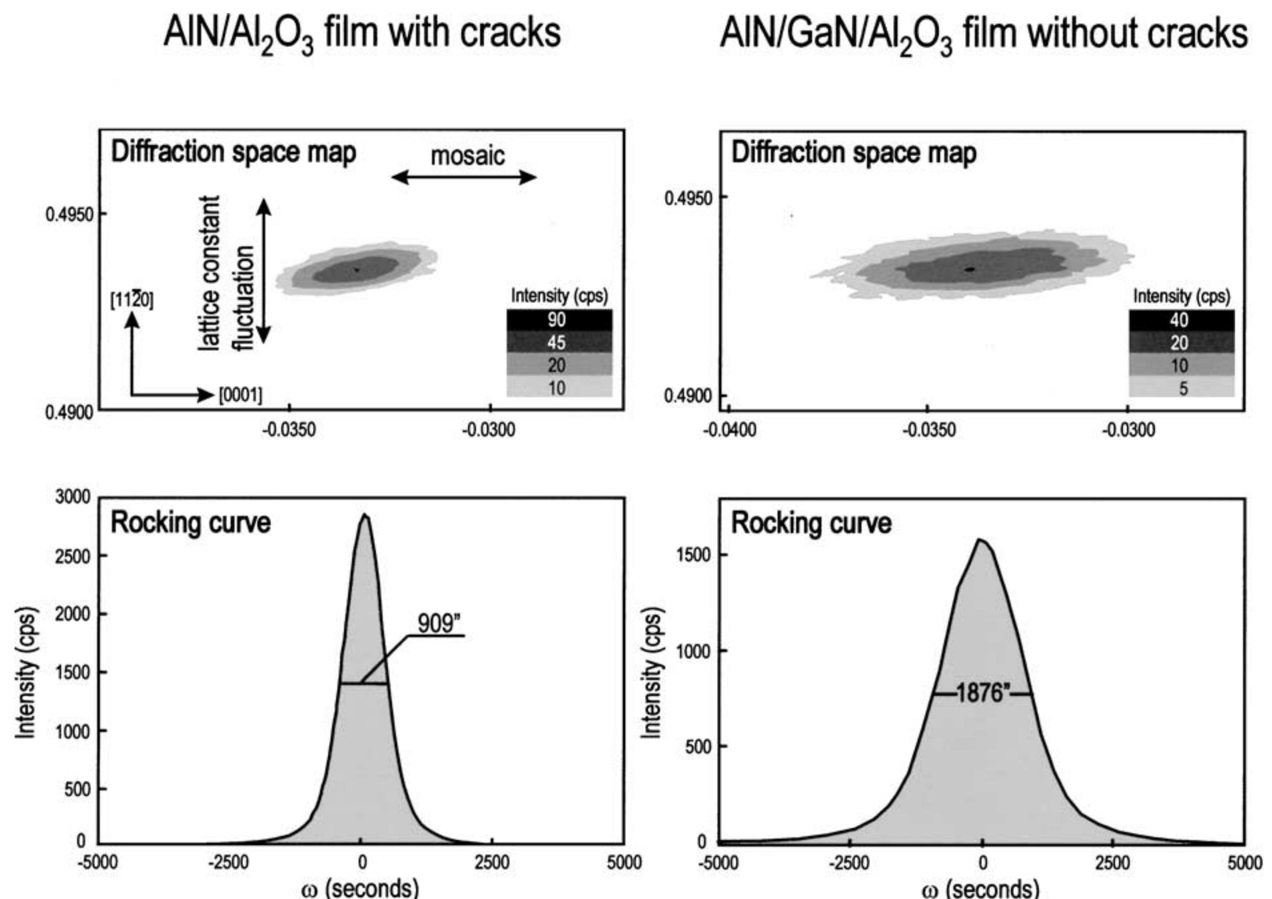

Figure 3 X-ray rocking curves and diffraction space maps of the AlN films with cracks (AlN/Al_2O_3 film) and without cracks ($AlN/GaN/Al_2O_3$ film) close to the $11\bar{2}0$ reflection. They were measured by aligning the $[0001]_{AlN}$ direction horizontal to the incident X-ray beam.

film with cracks, the curvature along the $[1\bar{1}00]_{AlN}$ direction can be interpreted by the thermal stress, but that along the $[0001]_{AlN}$ direction cannot.

3.2. Crystal structures

3.2.1. Crystallinity

Fig. 3 shows the X-ray rocking curves and the diffraction space maps of the AlN films. The coordinates of the diffraction space maps are normalized by the diameter of the Ewald sphere ($2/\lambda$, $\lambda = 0.15405$ nm). The shape of the reciprocal lattice points indicates that the rocking curves of AlN films are dominated by the mosaic structure rather than the fluctuation in the lattice constant [32]. Therefore, the full-width at half maximum (FWHM) corresponds to the degree of the mosaic structure formation. The FWHM due to the mosaic structure in the AlN film with cracks is only half of that for the AlN film without cracks.

3.2.2. Lattice parameters

Table II shows the absolute lattice parameters of the AlN films and the Al_2O_3 substrates. The values taken from Joint Committee on Powder Diffraction Standards

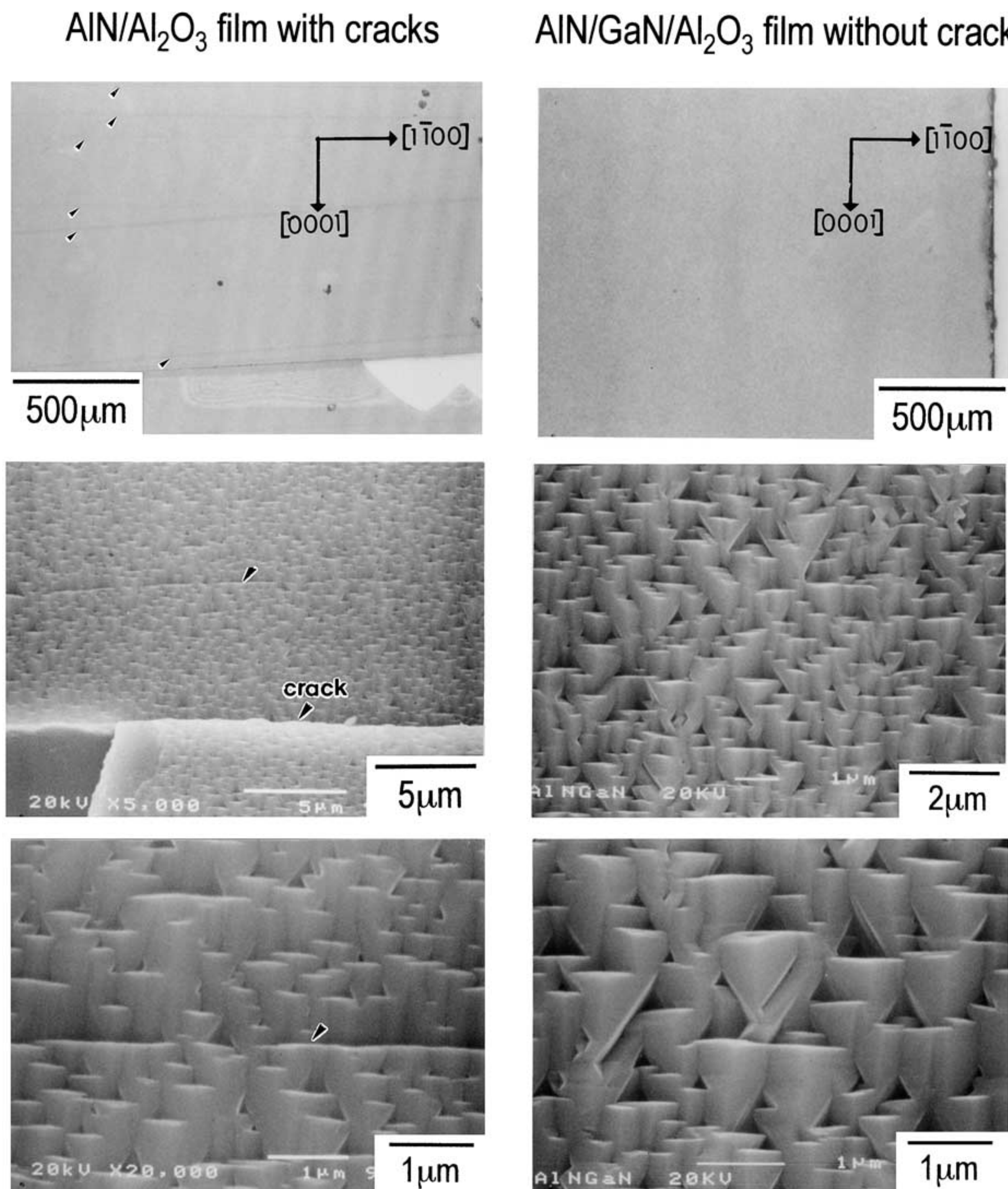

Figure 4 Surface morphological OM and SEM images of the AlN/Al_2O_3 epitaxial film with cracks and the $AlN/GaN/Al_2O_3$ epitaxial film without cracks.

(JCPDS) cards (No.25-1133, 42-1468) are also shown. The stress-free lattice parameters of both the AlN films and the Al_2O_3 substrates obtained from the X-ray powder diffraction profiles of ground specimens agree with the data on the JCPDS cards. The c-parameter of the AlN film with cracks is larger than that of the stress-free specimen, whereas that of the AlN film without cracks is smaller, which supports the results for the curvature of the wafers, i.e., the change in the c-parameters indicates that the tensile stress is induced along the $[0001]_{AlN}$ direction in the AlN film with cracks, whereas the compressive stress is induced in the AlN film without cracks.

3.3. Microstructures

3.3.1. Surface morphology

Fig. 4 shows the surface morphological OM and SEM images of the AlN films. Several lines parallel to the $[1\bar{1}00]_{AlN}$ direction, which are indicated by arrows, and exfoliation of the AlN film are observed on the surface of the AlN/Al_2O_3 film in the OM micrograph. The SEM micrographs reveal that the lines are identical to the AlN (0001) facets which align along the $[1\bar{1}00]_{AlN}$ direction. On the other hand, no lines are observed, and the AlN (0001) facets are random on the surface of the $AlN/GaN/Al_2O_3$ film without cracks.

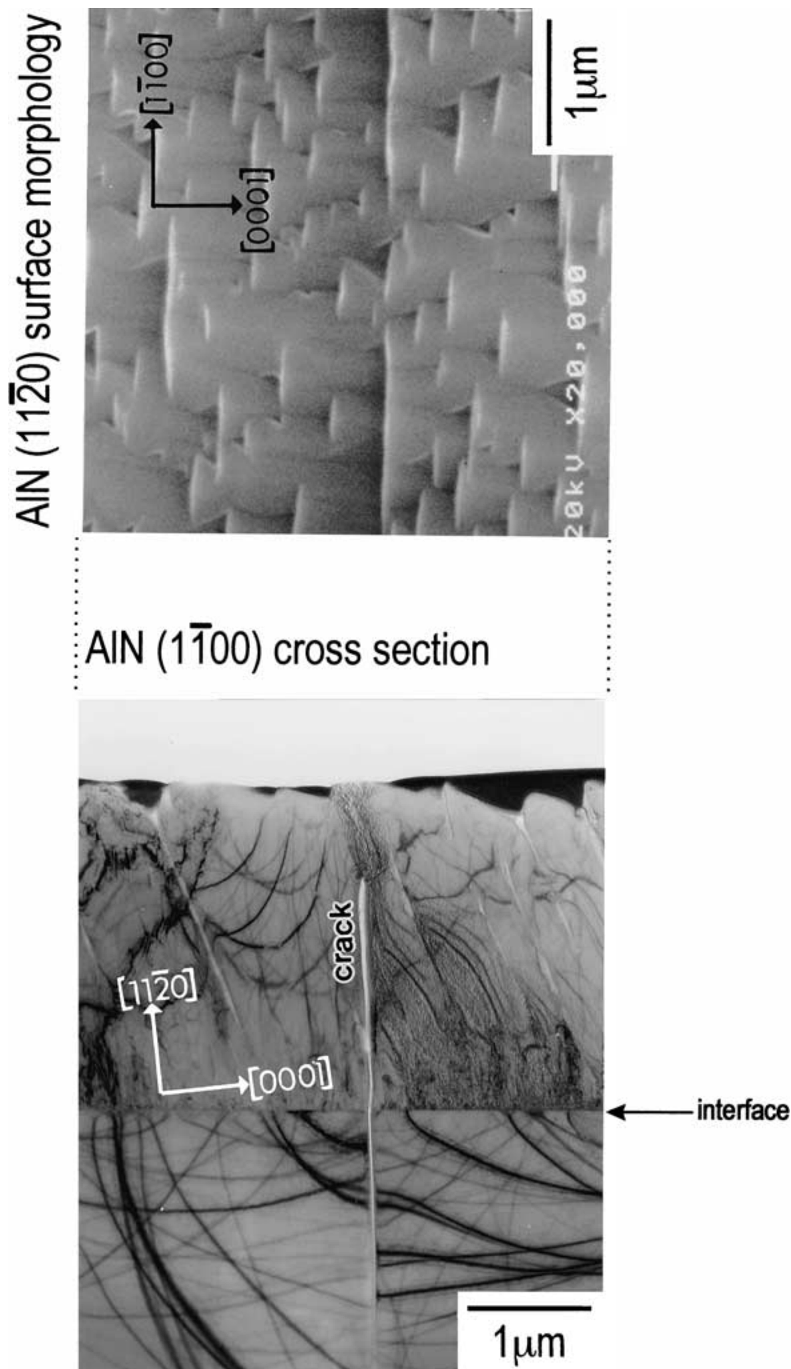

Figure 5 AlN(11$\bar{2}$0) surface morphological SEM image and AlN(1$\bar{1}$00) cross-sectional TEM image of the AlN/Al_2O_3 epitaxial film with cracks.

TABLE II Lattice parameters of AlN and Al_2O_3 for AlN/Al_2O_3 and $AlN/GaN/Al_2O_3$ films, stress-free lattice parameters obtained from ground specimens, and data on JCPDS cards

		Lattice parameters (nm)				
		AlN/Al_2O_3 film with cracks		$AlN/GaN/Al_2O_3$ film without cracks		
Material	Axis	Wafer	Stress-free	Wafer	Stress-free	JCPDS card
AlN film	*a*-axis	0.3114	0.3111	0.3115	0.3111	0.31114
	c-axis	0.4984	0.4978	0.4977	0.4978	0.49792
Al_2O_3 substrate	*a*-axis	0.4759	0.4759	0.4759	0.4759	0.47588
	c-axis	1.299	1.299	1.299	1.299	1.2992

3.3.2. Cross-sectional TEM images

Fig. 5 shows the AlN $(11\bar{2}0)$ surface morphological SEM image and the AlN $(1\bar{1}00)$ cross-sectional TEM image of the AlN/Al_2O_3 film. Cracks perpendicular to the interface between the film and the substrate are observed just below the film surface on which the AlN (0001) facets align along the $[1\bar{1}00]_{AlN}$ direction. The cracks extend about 1.7 μm from the interface to the AlN film and more than 2 μm into the Al_2O_3 substrate, but do not propagate to the AlN film surface. The tip of the cracks is the widest in the AlN film, and the cracks narrow as they penetrate deeply into the substrate, which indicates that the cracks are formed in the AlN film, and then propagate into the Al_2O_3 substrate.

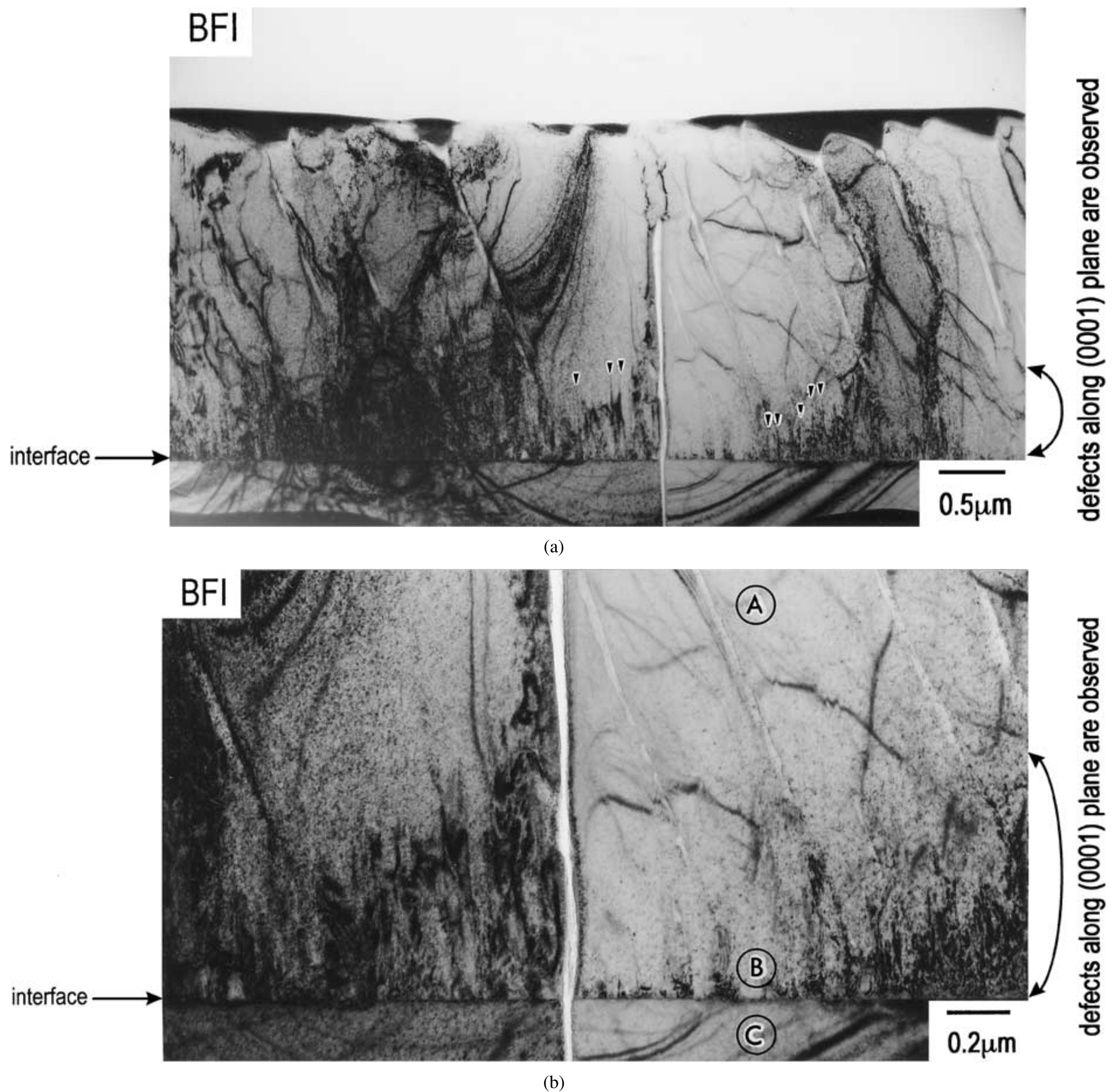

Figure 6 AlN $(1\bar{1}00)$ cross-sectional bright-field TEM images of the AlN/Al_2O_3 heteroepitaxial film with cracks. (a) low-magnification image, and (b) high-magnification image at the interface region. Symbols (▼) indicate the planar imperfections induced in the $(0001)_{AlN}$ plane. The defects disappear at a film thickness of about 0.8 μm.

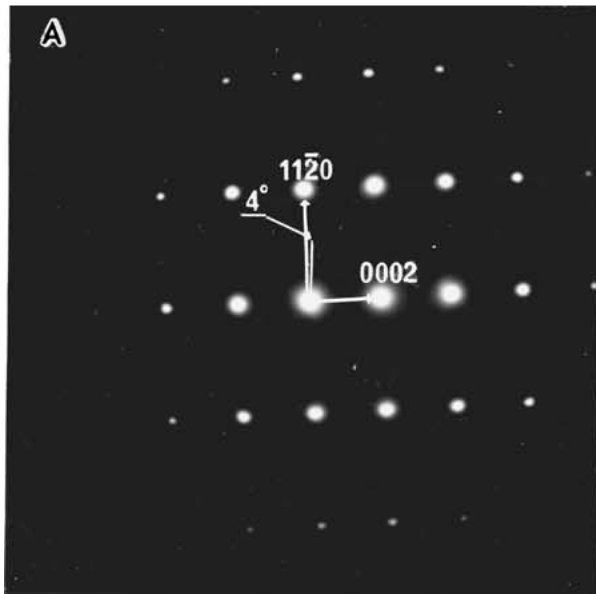

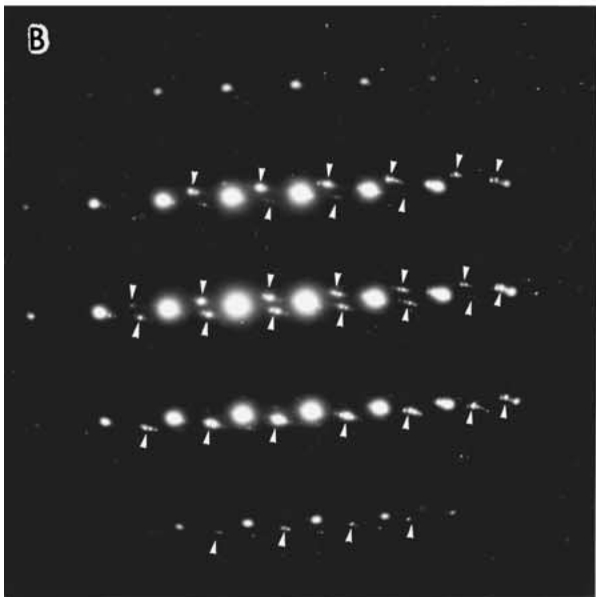

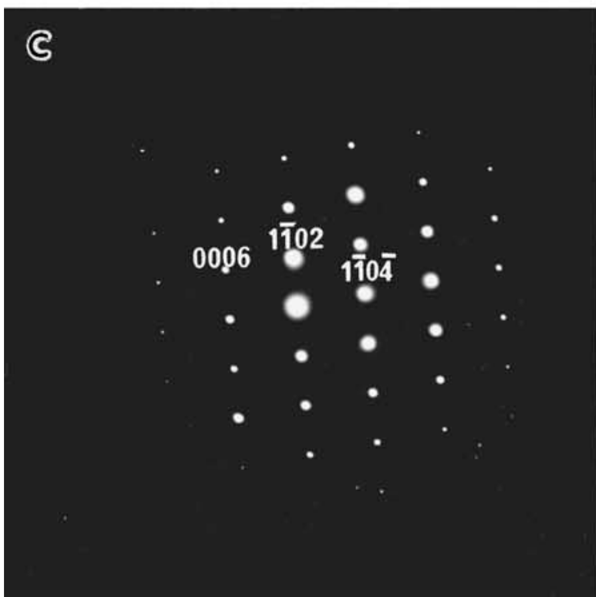

Figure 7 Electron diffraction patterns of the AlN/Al_2O_3 heteroepitaxial film with cracks. The electron diffraction patterns were taken at regions A, B and C indicated in Fig. 6b, respectively. Symbols (△ and ▽) indicate electron diffraction spots other than those due to the AlN epitaxial film, indicating that another crystal phase grows close to the interface.

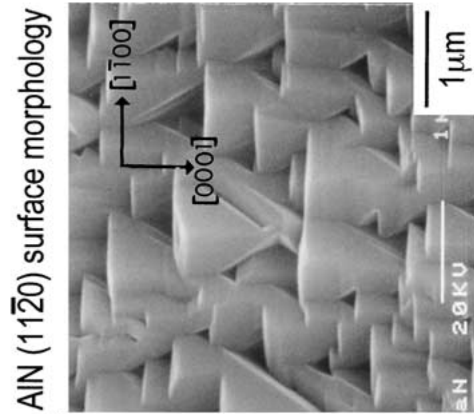

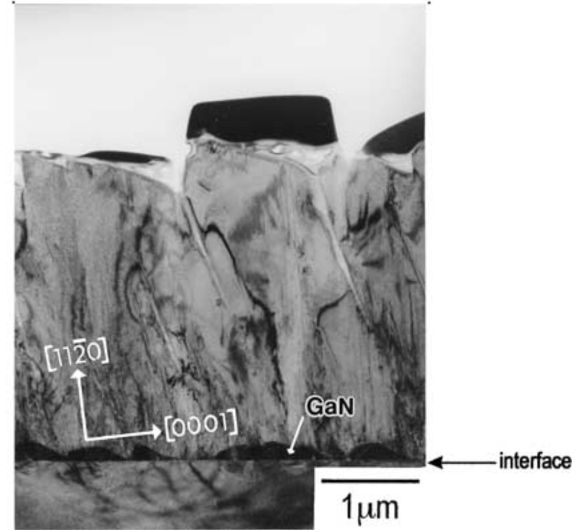

Figure 8 AlN(11$\bar{2}$0) surface morphological SEM image and AlN(1$\bar{1}$00) cross-sectional TEM image of an $AlN/GaN/Al_2O_3$ epitaxial film without cracks.

Fig. 6 shows the AlN (1$\bar{1}$00) cross-sectional bright-field TEM images. Defects along the $(0001)_{AlN}$ plane, which propagate from the interface to the AlN film, are observed. It appears that the lattice mismatch along the $[0001]_{AlN}$ direction is relaxed by the planar imperfections induced in the $(0001)_{AlN}$ plane. However, the defects disappear at a film thickness of about 0.8 μm. Fig. 7 shows the electron diffraction patterns obtained at regions A (AlN film), B (AlN film close to interface) and C (Al_2O_3 substrate) shown in Fig. 6b, respectively. The electron diffraction patterns A and C show that the (11$\bar{2}$0)-oriented AlN single crystals have grown epitaxially on the (1$\bar{1}$02) α-Al_2O_3 substrate. However, many electron diffraction spots other than those of the AlN epitaxial film are observed close to the interface (electron diffraction pattern B). The additional spots are situated at about 10° clockwise from the $[0001]_{AlN}$ direction, and multiple diffraction spots are also observed. The interplanar spacings (d-spacings) calculated from the additional spots do not agree with those of the AlN crystal. Therefore, the electron diffraction pattern suggests that another crystal phase grows close to the interface and that the lattice constants and crystallographic directions are different from those of the

AlN epitaxial phase, although we could not interpret the phase fully. However, the other phase is not observed when the thickness exceeds about 0.2 μm.

Fig. 8 shows the AlN $(11\bar{2}0)$ surface morphological SEM image and the AlN $(1\bar{1}00)$ cross-sectional TEM image of the AlN/GaN/Al_2O_3 film. The GaN buffer layer, which is shaped like an island, is observed at the interface between the AlN film and the Al_2O_3 substrate. Fig. 9 shows the AlN $(1\bar{1}00)$ cross-sectional bright-field TEM images. The defects along the $(0001)_{AlN}$ plane, which occur at the interface between the GaN buffer layer and the Al_2O_3 substrate, propagate into the AlN film. The defects are longer than those in the AlN/Al_2O_3 film with cracks, and several defects propagate to the AlN film surface. The TEM images correspond to the results of HR-XRD which indicate that the crystallinity of the AlN/GaN/Al_2O_3 film is worse than that of the AlN/Al_2O_3 film. Fig. 10 shows the electron diffraction patterns obtained at regions D (AlN film), E (interface of AlN and GaN) and F (Al_2O_3 substrate) shown in Fig. 9b, respectively. The electron diffraction patterns show that the $(11\bar{2}0)$-oriented AlN and GaN single crystals grow epitaxially on the $(1\bar{1}02)$ α-Al_2O_3 substrate. No additional electron diffraction spots are observed in both the AlN film and the GaN buffer layer.

3.4. Mechanism of cracking

Table III shows the summarized experimental results obtained in this study. The discussion will focus on (1) the process of cracking, and (2) the role of the GaN buffer layer.

3.4.1. Process of cracking

Considering the curvature of the wafer and the c-parameter of the AlN film, it may be stated that the tensile stress is induced along the $[0001]_{AlN}$ direction in the AlN film with cracks. The average stress σ_0 in the film can be calculated from the radius of curvature R using

$$\sigma_0 = \frac{E_s}{1-\nu_s} \cdot \frac{t_s^2}{6Rt_f}, \tag{1}$$

where E_s, ν_s, t_f and t_s are the Young's modulus (380 GPa), the Poisson's ratio (0.25) of the Al_2O_3 substrate, the film thickness (2–3 μm) and the substrate thickness (430 μm), respectively. The stress hardly varies in the film before cracking [21], since the film is far thinner than the substrate. However, the stress changes to the opposite sign abruptly at the interface of the film and the substrate. Here, we estimate the stress σ_G in the film during the growth. The thermal stress σ_T can be calculated as

$$\sigma_T = \frac{E_f}{1-\nu_f} \cdot \Delta\alpha \cdot \Delta T, \tag{2}$$

where $\Delta\alpha$ is the difference between the thermal expansion coefficients of the film and the substrate, and ΔT is the difference between the growth temperature and room temperature. The stress σ_G in the film just before the end of growth can be estimated:

$$\sigma_G = \sigma_0 - \sigma_T. \tag{3}$$

Using these equations, in the AlN/Al_2O_3 film, the tensile stress σ_G of 850 MPa and 2010 MPa is obtained along the $[1\bar{1}00]_{AlN}$ and $[0001]_{AlN}$ directions, respectively. Thus, it is found that the tensile stress is induced along both directions during the growth, and that the value of the tensile stress along the $[0001]_{AlN}$ direction is more than twice that along the $[1\bar{1}00]_{AlN}$ direction. In brittle materials such as AlN, cracks may occur easily under tensile stress which exceeds a critical value. The TEM observation in which the tip of the cracks is widest in the AlN film suggests that the cracks are formed in the AlN film. Therefore, it can be concluded that the cracks are induced by the tensile stress along the $[0001]_{AlN}$ direction.

The origin of the tensile stress which induces the cracks is described briefly. The origin of the stress in a thin film involves the annihilation of lattice defects [33]. Volume shrinkage is associated with the annihilation of lattice defects during film growth, and it leads to tensile stress in the film when the film is attached to a substrate. From the TEM images, it is evident that

TABLE III Summarized experimental results of the crystal structure and microstructure of AlN/Al_2O_3 and AlN/GaN/Al_2O_3 films obtained in this study

	Summarized experimental results	
Item investigated in this study	AlN/Al_2O_3 epitaxial film	AlN/GaN/Al_2O_3 epitaxial film
Cracks	• Parallel to $[1\bar{1}00]$ direction and perpendicular to interface • They do not propagate to surface • They are the widest in AlN film	None
Curvature of wafer	$[1\bar{1}00]$ direction Convex [0001] direction Concave	Convex Convex
Crystallinity of AlN	Better	Worse
Lattice parameter of AlN (c-axis)	>Stress-free value	<Stress-free value
Surface morphology	(0001) facets align along $[1\bar{1}00]$ direction just above cracks	Random facets
Orientation	Another crystal phase close to interface	Epitaxial
Defect induced in $(0001)_{AlN}$ plane	Annihilation at 0.8 μm	Propagation to surface

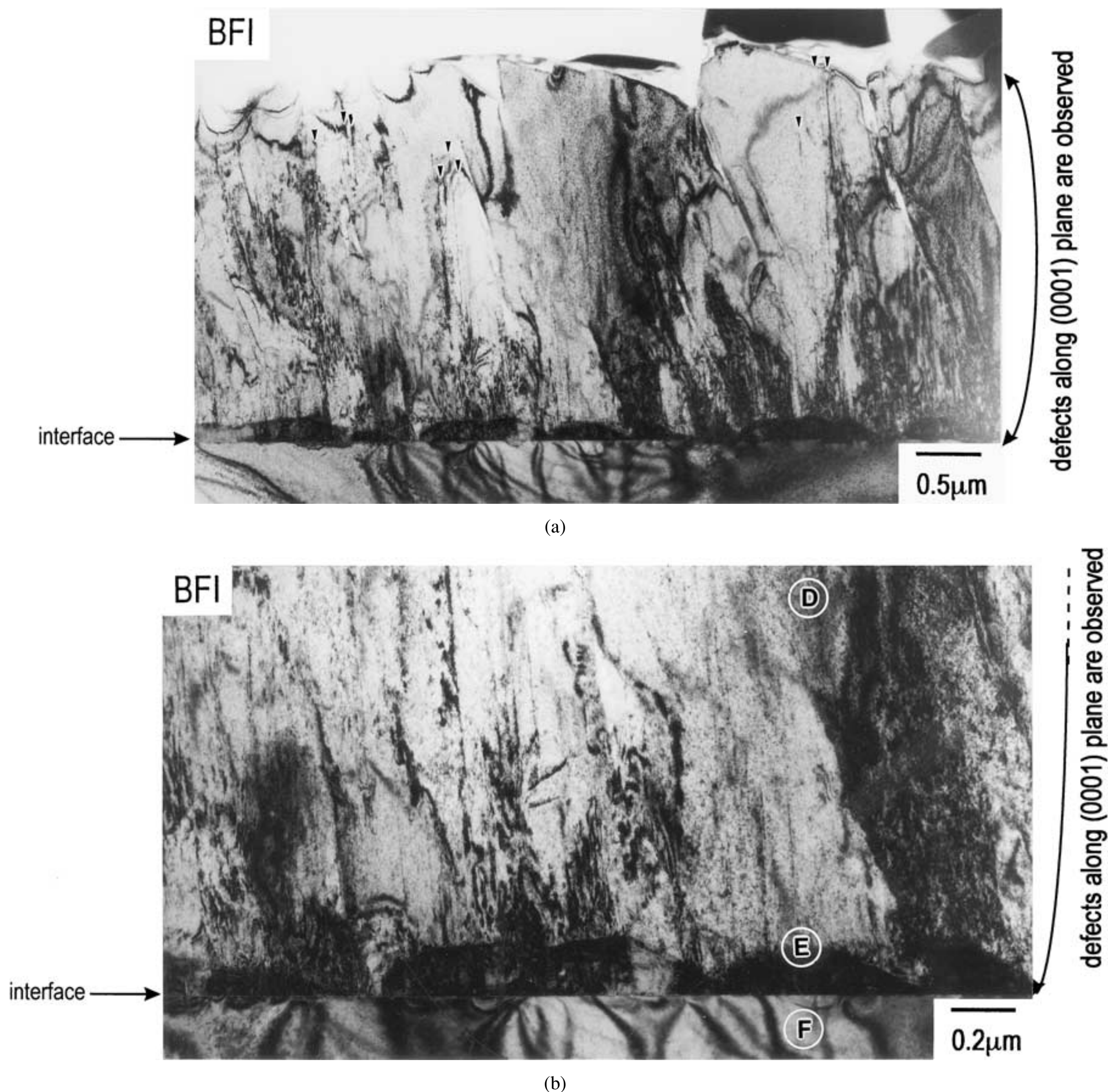

Figure 9 AlN (1$\bar{1}$00) cross-sectional bright-field TEM images of the AlN/GaN/Al_2O_3 heteroepitaxial film without cracks. (a) low-magnification image, and (b) high-magnification image at the interface region. Symbols (▼) indicate the planar imperfections induced in the $(0001)_{AlN}$ plane. Several defects propagate to the surface.

the lattice mismatch of the AlN film and the Al_2O_3 substrate along the $[0001]_{AlN}$ direction is relaxed by the defects along the $(0001)_{AlN}$ plane and/or another crystal phase. However, the defects and another crystal phase in the AlN/Al_2O_3 film disappear as the AlN film grows. The tensile stress is induced by the annihilation of the defects along the $(0001)_{AlN}$ plane and/or another crystal phase.

It should be mentioned that the cracks do not propagate to the surface of the AlN film under the homogeneous tensile stress, although the cracks propagate into the Al_2O_3 substrate under the compressive stress. These observations suggest that the cracks are formed during the epitaxial growth. The cracks are closed since the source gas continues to be supplied even after cracking. While the cracks are closed, they function as a crystal boundary; as a consequence, the AlN (0001) facets align along the $[1\bar{1}00]_{AlN}$ direction just above the cracks.

On the basis of these results and discussion, the process of cracking may be concluded to be as follows. The cracks are formed in the AlN film due to the tensile stress along the $[0001]_{AlN}$ direction during the epitaxial growth, and simultaneously propagate to the AlN film surface and into the Al_2O_3 substrate. The tensile stress is induced by the annihilation of the defects along the $(0001)_{AlN}$ plane and/or another crystal phase.

3.4.2. Role of GaN buffer layer

Contrary to the AlN/Al_2O_3 film with cracks, in the AlN/GaN/Al_2O_3 film without cracks, it appears that the compressive stress along the $[0001]_{AlN}$ direction is induced in the AlN film at room temperature, i.e., the wafer is under thermal stress. Since the growth conditions of the AlN/GaN/Al_2O_3 film, except for the GaN buffer layer, were the same as those of the AlN/Al_2O_3 film, the suppression of the tensile stress along the $[0001]_{AlN}$ direction is attributable to the GaN layer.

The important TEM observations for discussing the role of the GaN buffer layer are that: (1) the defects along the $(0001)_{AlN}$ plane in the AlN/GaN/Al_2O_3 film

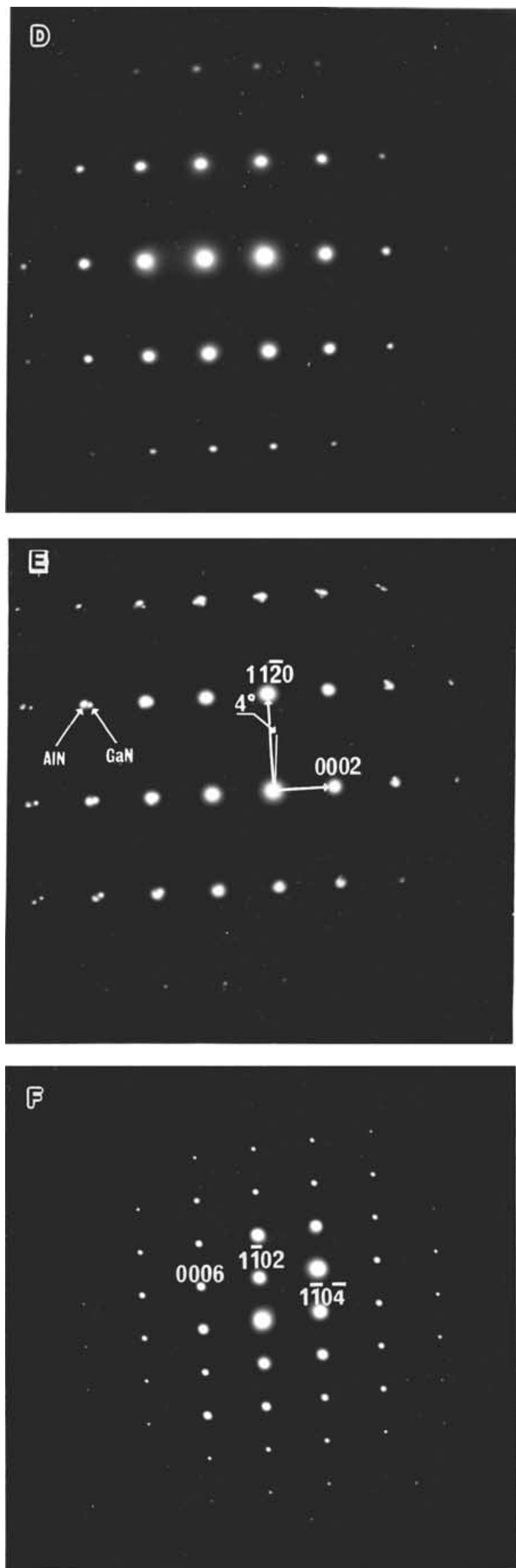

Figure 10 Electron diffraction patterns of the AlN/GaN/Al_2O_3 heteroepitaxial film without cracks. The electron diffraction patterns were taken at regions D, E and F indicated in Fig. 9b, respectively. Both the AlN film and the GaN buffer layer are grown epitaxially on the Al_2O_3 substrate.

without cracks are longer than those in the AlN/Al_2O_3 film with cracks, and that (2) both AlN and GaN crystals are grown epitaxially in the AlN/GaN/Al_2O_3 film, whereas another crystal phase grows close to the interface in the AlN/Al_2O_3 film. In the AlN/GaN/Al_2O_3 film, the observations indicate that the defects continue to propagate with the growth of the AlN film, and that the generation of another crystal phase is suppressed. As a consequence of the role of the GaN buffer layer, it appears that the tensile stress is suppressed and no cracks occur in the AlN/GaN/Al_2O_3 film. We believe that it will be worthwhile to analyze the role of the GaN buffer layer more closely.

4. Summary

The cracking mechanism in AlN($11\bar{2}0$)/α-Al_2O_3 ($1\bar{1}02$) heteroepitaxial film grown by MOCVD was discussed on the basis of the results of HR-XRD and OM, SEM and TEM observations. In the AlN/Al_2O_3 film, cracks are formed in the AlN film due to tensile stress along the $[0001]_{AlN}$ direction during the epitaxial growth, and simultaneously propagate to the AlN film surface and into the Al_2O_3 substrate. The tensile stress is induced by the annihilation of the defects along the $(0001)_{AlN}$ plane and/or another crystal phase. On the other hand, in the AlN/GaN/Al_2O_3 film, the defects continue to propagate with the growth of the AlN film, and the generation of another crystal phase is suppressed; as a consequence of the existence of the GaN buffer layer, it appears that the tensile stress is suppressed and no cracks occur.

Acknowledgement

We thank Mr. Takuma Makino of NGK Insulators for discussing the stress distribution in the AlN/Al_2O_3 epitaxial film.

References

1. K. TSUBOUCHI and N. MIKOSHIBA, *IEEE Trans. Sonics Ultrason.* **SU-32** (1985) 634.
2. H. M. MANASEVIT, F. M. ERDMANN and W. I. SIMPSON, *J. Electrochem. Soc.* **118** (1971) 1864.
3. W. M. YIM, E. J. STOFKO, P. J. ZANZUCCHI, J. I. PANKOVE, M. ETTENBERG and S. L. GILBERT, *J. Appl. Phys.* **44** (1973) 292.
4. M. T. DUFFY, C. C. WANG, G. D. O'CLOCK, JR., S. H. MCFARLANE III and P. J. ZANZUCCHI, *J. Electron. Mater.* **2** (1973) 359.
5. G. D. O'CLOCK, JR. and M. T. DUFFY, *Appl. Phys. Lett.* **23** (1973) 55.
6. J. K. LIU, R. B. STOCKS and K. M. LAKIN, in Proceedings of the 1975 IEEE Ultrasonic. Symp. 1975, p. 234.
7. M. MORITA, N. UESUGI, S. ISOGAI, K. TSUBOUCHI and N. MIKOSHIBA, *Jpn. J. Appl. Phys.* **20** (1981) 17.
8. H. KAWAKAMI, K. SAKURAI, K. TSUBOUCHI and N. MIKOSHIBA, *ibid.* **27** (1988) L161.
9. S. KANEKO, M. TANAKA, K. MASU, K. TSUBOUCHI and N. MIKOSHIBA, *J. Cryst. Growth* **115** (1991) 643.
10. C. J. SUN, P. KUNG, A. SAXLER, H. OHSATO, K. HARITOS and M. RAZEGHI, *J. Appl. Phys.* **75** (1994) 3964.
11. K. MASU, Y. NAKAMURA, T. YAMAZAKI, T. SHIBATA, M. TAKAHASHI and K. TSUBOUCHI, *Jpn. J. Appl. Phys.* **34** (1995) L760.
12. F. BUGGE, A. N. EFIMOV, I. G. PICHUGIN, A. M. TSAREGORODTSEV and M. A. CHERNOV, *Cryst. Res. Technol.* **22** (1987) 65.

13. K. KAYA, Y. KANNO, H. TAKAHASHI, Y. SHIBATA and T. HIRAI, *Jpn. J. Appl. Phys.* **35** (1996) 2782.
14. K. KAYA, H. TAKAHASHI, Y. SHIBATA, Y. KANNO and T. HIRAI, *ibid.* **36** (1997) 2837.
15. H. OKANO, N. TANAKA, Y. TAKAHASHI, T. TANAKA, K. SHIBATA and S. NAKANO, *Appl. Phys. Lett.* **64** (1994) 166.
16. H. OKANO, N. TANAKA, Y. HIRANO, Y. KOBAYASHI, K. SHIBATA and S. NAKANO, *Jpn. J. Appl. Phys.* **33** (1994) 2957.
17. S. YOSHIDA, S. MISAWA and A. ITOH, *Appl. Phys. Lett.* **26** (1975) 461.
18. S. YOSHIDA, S. MISAWA, Y. FUJII, S. TANAKA, H. HAYAKAWA, S. GONDA and A. ITOH, *J. Vac. Sci. Technol.* **16** (1979) 990.
19. R. A. LAGAN and C. D. THURMOND, *J. Electrochem. Soc.* **119** (1972) 1727.
20. T. MATSUMOTO and M. AOKI, *Jpn. J. Appl. Phys.* **13** (1974) 1583.
21. N. ITOH and J. C. RHEE, *J. Appl. Phys.* **58** (1985) 1828.
22. T. DETCHPROHM, K. HIRAMATSU, K. ITOH and I. AKASAKI, *Jpn. J. Appl. Phys.* **31** (1992) L1454.
23. K. HIRAMATSU, T. DETCHPROHM and I. AKASAKI, *ibid.* **32** (1993) 1528.
24. H. AMANO, M. IWAYA, T. KASHIMA, M. KATSURAGAWA, I. AKASAKI, J. HAN, S. HEARNE, J. A. FLORO, E. CHASON and J. FIGIEL, *ibid.* **37** (1998) L1540.
25. G. STEUDE, B. K. MEYER, A. GOLDNER, A. HOFFMANN, A. KASHUNER, F. BECHSTEDT, H. AMANO and I. AKASAKI, *ibid.* **38** (1999) L498.
26. T. SHIBATA, Y. HORI, K. ASAI, Y. NAKAMURA, M. TANAKA, K. KAIGAWA, J. SHIBATA and H. SAKAI, in Proceedings of the International Workshop on Nitride Semiconductors IPAP Conf. Series 1, 2000, p. 981.
27. P. KUNG, C. J. SUN, A. SAXLER, H. OHSATO and M. RAZEGHI, *J. Appl. Phys.* **75** (1994) 4515.
28. I. AKASAKI, K. HIRAMATSU and H. AMANO, in "Memoirs of Faculty of Engineering, Nagoya University," Vol. 43 (Nagoya University, Japan, 1991) p. 147.
29. W. J. BARTELS, *J. Vac. Sci. Technol.* **B1** (1983) 338.
30. P. F. FEWSTER and N. L. ANDREW, *J. Appl. Crystallogr.* **28** (1995) 451.
31. H. TORAYA, *ibid.* **19** (1986) 440.
32. P. F. FEWSTER, in "X-ray and Neutron Dynamical Diffraction: Theory and Applications," edited by Authier (Plenum Press, New York, 1996) p. 269.
33. H. S. STORY and R. W. HOFFMAN, *Proc. Phys. Soc.* **B70** (1957) 950.

Received 12 September 2000
and accepted 21 May 2001